

# **The infiltration behavior and chemical compatibility of molten lead-bismuth eutectic in nuclear graphite at elevated temperature**

Zhao He<sup>a, b, c</sup>, Zhanjun Liu<sup>a, b \*</sup>, T. James Marrow<sup>c</sup>, Jinliang Song<sup>d</sup>

<sup>a</sup> Key Laboratory of Carbon Materials, Institute of Coal Chemistry, Chinese Academy of Sciences, Taiyuan 030001, China

<sup>b</sup> Center of Materials Science and Optoelectronics Engineering, University of Chinese Academy of Sciences, Beijing 100049, China

<sup>c</sup> Department of Materials, University of Oxford, Oxford OX1 3PH, UK

<sup>d</sup> Shanghai Institute of Applied Physics, Chinese Academy of Sciences, Shanghai 201800, China

## **Abstract**

Six grades of commercial nuclear graphite of different microstructures (NBG-17, NBG-18, NBG-25, IG-110, NGCT-50 and ZXF-5Q) were infiltrated with molten lead-bismuth eutectic (LBE) at 800 °C and a series of pressures to evaluate their barrier property to molten LBE. Molten LBE infiltration caused a decrease of the (002) interlayer spacing and an increase of mean crystallite dimension perpendicular to the (002) diffracting plane. This is ascribed to compressive stress evolution from the infiltration and subsequent solid-state phase transformation of LBE. One representative graphite (IG-110) was immersed in molten LBE at 800 °C for 1000 hours and no evidence of corrosion was detected, which has preliminarily verified the chemical stability of graphite in molten LBE. This work indicates that nuclear graphite with small pores has great chance to act as coolant channel material for compact high temperature reactor.

**Keywords:** Compact high temperature reactor, Nuclear graphite, Lead-bismuth eutectic, Infiltration

---

\* Corresponding authors  
E-mail address: zjliu03@sxicc.ac.cn (Zhanjun Liu)

behavior, Barrier property, Chemical compatibility

## 1. Introduction

The compact high temperature reactor (CHTR) is seen as a key platform and being developed to verify advanced technologies related to high temperature nuclear reactors such as production of hydrogen [1]. Lead-bismuth eutectic (LBE, Pb44.5-Bi55.5, wt%) is a promising coolant for the CHTR concept. We are developing a prototype CHTR, which is designed for special applications. Molten LBE acts as coolant and flows in the prototype CHTR circuit in pressurized condition (several atmospheric pressure), which is conducive to promoting the removal of core heat and upgrading the reactor efficiency. In our prototype CHTR, the pore size of graphite coolant channels should be small enough to prevent molten LBE in pressurized condition from infiltrating and even leaking out, which can reduce the accumulation of radioactive nuclides in graphite coolant channels and also ensure the normal operation of reactor. In view of the porous nature of nuclear graphite, the infiltration of molten LBE into the graphite coolant channels is a significant concern. Moreover, molten LBE has been shown to be highly corrosive of structural materials such as high-entropy alloy [2] and ferritic alloy [3], so the corrosion of the graphite coolant channels is a significant concern too, although nuclear graphite has high chemical stability and high temperature mechanical strength. For the development of CHTR, it is necessary to study the infiltration behavior and chemical compatibility of molten LBE in commercial nuclear graphite at elevated temperature.

Many studies on the infiltration behavior of molten salt in nuclear graphite have been reported in recent years [4-12]. Additionally, the effects of molten salt infiltration on chemical bonding [13, 14], stacking order [15], thermal expansion behavior [16] and strength [17] of nuclear graphite have also been reported. However, the interactions between molten LBE and nuclear graphite have been rarely

reported. The infiltration of numerous grades of graphite by molten LBE was studied for a proposed USA liquid metal fuel reactor [18, 19], and a compatibility test between molten LBE and graphite showed graphite was not corroded by molten LBE under the experimental conditions [20]. However, it has been reported that graphite can be corroded by molten LBE to form a  $\text{PbC}_2$  reaction layer at the interface [21], and that SiC coating is effective to protect graphite from attack by molten LBE [22]. The infiltration behavior and chemical compatibility of molten LBE in commercial nuclear graphite at elevated temperatures have not been systematically reported until now, so it is imperative and urgent to carry out related research for the development of CHTR.

In this study, molten LBE infiltration experiments were conducted on a series of commercial nuclear graphites. The distribution and morphology of LBE infiltration in graphite was observed. And the molten LBE infiltration experiments were compared with mercury intrusion. The variations of the (002) diffraction peak position and full width at half maximum (FWHM) before and after the molten LBE infiltration experiments were adopted to investigate and analyze the influence of the infiltration process on the crystal structure of graphite. The mechanism for changes in the crystal structure of graphite is proposed from the perspective of compressive stress caused by the infiltration and the subsequent solid-state phase transformation of LBE. To investigate the stability of graphite in molten LBE, chemical compatibility testing was also carried out by immersion of one representative graphite (IG-110) in molten LBE at 800 °C for 1000 hours.

## **2. Experimental**

### ***2.1. Materials***

The commercial graphite materials used were NBG-17, NBG-18 and NBG-25 from SGL Carbon Group, IG-110 from Toyo Tanso Co., Ltd, NGCT-50 from Chengdu Carbon Co., Ltd, and ZXF-5Q

from Poco Graphite. These six grades of graphite were selected in this work because of their wide range of pore size. Basic information on filler type, grain size, density and forming process is listed in Table 1. Graphite samples with diameter of 10 mm and height of 20 mm were obtained from corresponding graphite bulks by machining, marked by a laser marking machine, successively cleaned by ultrasound in alcohol and distilled water to remove adherent contaminants, and finally dried in a vacuum oven at 120 °C for 24 hours. The LBE used as impregnant had an impurity content of less than 100 ppm.

Table 1 – Graphite filler type, grain size, density and forming process.

Grade	Filler type	Grain size (μm)	Bulk density (g/cm <sup>3</sup> )	Forming process
NBG-17	Pitch	Max. 800	1.89	Vibration molding
NBG-18	Pitch	Max. 1600	1.85	Vibration molding
NBG-25	Petroleum	Max. 60	1.82	Vibration molding
IG-110	Petroleum	20	1.77	Isostatic molding
NGCT-50	Pitch	5	1.79	Isostatic molding
ZXF-5Q	Unknown	1	1.78	Isostatic molding

## 2.2. Molten LBE infiltration

The infiltration experiments were conducted in a pressure vessel installed in an argon-filled glove box, and the graphite samples were degassed by a vacuum pump before each infiltration experiment. The schematic of the experimental setup for molten LBE infiltration, the photograph of sample holder and the specific operation process have been depicted in previous work [23]. The infiltration experiments were conducted at 800 °C under a series of infiltration pressures (1, 3, 5, 8, 10, 15 and 20 atm), each with a duration of 24 hours. After the infiltration experiment, the residual LBE film adhering

to the sample surfaces was removed by wiping with a mixed solution of hydrogen peroxide, acetic acid and ethanol in the volume ratio of 1:1:1 [24]. The weight gain ratio ( $\eta$ , wt%) for each graphite sample was evaluated using equation (1),

$$\eta = (m_2 - m_1) / m_1 \quad (1)$$

where  $m_1$  and  $m_2$  refer to the weight of the graphite sample before and after the infiltration treatment, respectively.

### **2.3. Chemical compatibility**

IG-110 was selected as the representative nuclear graphite for the LBE compatibility experiment, which was also performed in the pressure vessel within the argon-filled glove box. The experiment was carried out under normal pressure and the graphite samples (discs with diameter of 10 mm and height of 2 mm) were not degassed before immersion in static molten LBE at 800 °C for 1000 hours.

### **2.4. Characterization methods**

A field emission scanning electron microscope (SEM, JSM-7001F) equipped with an energy dispersive spectrometer (EDS, Oxford Instruments Inca Energy 250, X-Act SDD detector) was adopted to characterize the sample microstructures and the LBE distribution within the microstructure, by observation of fracture surfaces. A high vacuum furnace (VAF-30, working at around  $10^{-3}$  Pa) equipped with a high-temperature microscope (DH-HV 1303UM) was used to measure the contact angle between molten LBE and graphite at 800 °C by the sessile drop method [25, 26], using a mechanically polished IG-110 sample (10×10×2 mm) as the substrate. An automatic mercury porosimeter (AutoPore IV 9500) was adopted to obtain the pore structural information. X-ray diffraction (XRD, Bruker D8 Advance) was used to characterize the phase composition and crystal phase structure of samples at 25 °C, using an X-ray wavelength of 0.15406 nm (Cu,  $K_\alpha$ ). Silicon

powder (NIST SRM 640e) was used as the standard sample to determine the instrumental broadening, which was tested to be 0.2369 degree in this work and then subtracted using variance subtraction by referring to equation (2),  $\beta^2 = \beta_N^2 - \beta_I^2$  (2) [27], where  $\beta_N$  is the FWHM of the sample peak and  $\beta_I$  is the instrumental broadening from the standard sample. Meanwhile, silicon powder was also used as standard sample to revise and determine the peak location and FWHM of graphite sample.

### **3. Results and discussion**

#### **3.1 Graphite Microstructure**

Fig. 1 shows fracture surface images of these six grades of graphite. There are many large pores with size of tens of microns distributed in NBG-17 and NBG-18 (Fig. 1a and b). With decreasing filler grain size, the pore size decreases to a few microns in NBG-25 and IG-110 (Fig. 1c and d). As filler grain size decreases further (ultrafine grain level) in NGCT-50 and ZXF-5Q, the structures are more compact with pores of near and even less than 1  $\mu\text{m}$  (Fig. 1e and f). The pore size difference of these six grades of graphite will greatly affect their subsequent molten LBE infiltration results.

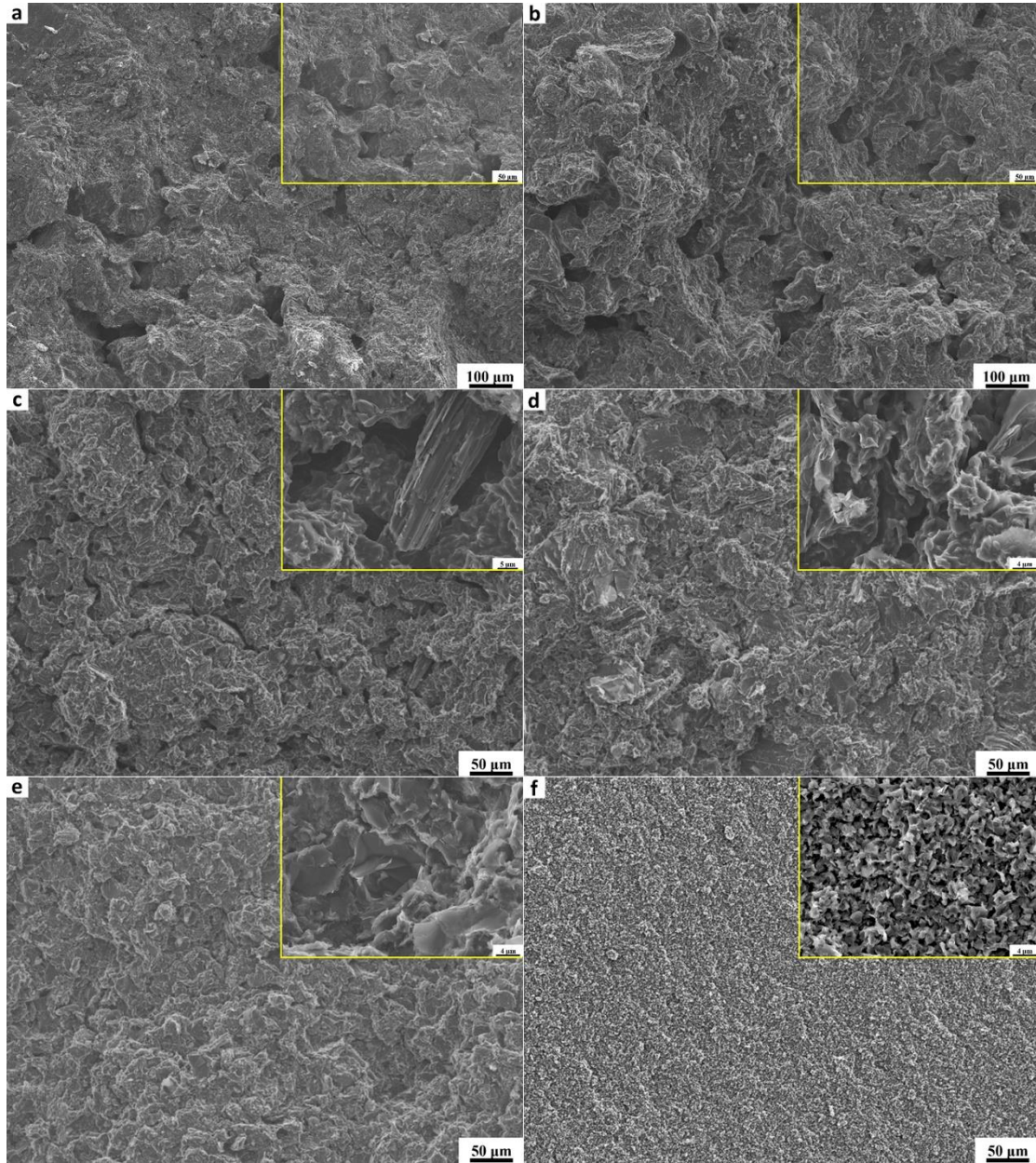


Fig. 1 – Fracture surface images: a) NBG-17; b) NBG-18; c) NBG-25; d) IG-110; e) NGCT-50; and f) ZXF-5Q. (Insets are higher magnification images).

### 3.2. Molten LBE and mercury infiltration into graphite

Fig. 2a shows the molten LBE weight gain ratio obtained at different pressures and 800°C. For NBG-17 and NBG-18, molten LBE infiltrates easily and their weight gain ratios at 1 atm are as high as 14.75 wt% and 14.44 wt%, respectively. With the increase of infiltration pressure, their weight gain ratios increase gradually and tend to saturate at 8 atm with values reaching 20.59 wt% and 23.62 wt%,

respectively. NBG-25 and IG-110 exhibit relatively better barrier property, with weight gain ratios at 1 atm of 1.82 wt% and 1.88 wt%, respectively. Their weight gain ratios tend to saturate at 5 atm with values reaching 29.68 wt% and 42.82 wt%, respectively. For NGCT-50, molten LBE infiltration is difficult at pressures less than 5 atm, but its weight gain ratio tends to saturate at 10 atm with value reaching 36.81 wt%. The saturated weight gain rates of these five grades of graphite indicate that their open pores are filled with molten LBE. In contrast, ZXF-5Q shows a low weight gain ratio of less than 0.12 wt% even at 20 atm, which demonstrates a superior barrier property to molten LBE. The contact angle between molten LBE and graphite at 800 °C is about 118° (Fig. 2b), which indicates that molten LBE cannot wet graphite well. To infiltrate molten LBE into graphite, molten LBE needs to flow into the pores of graphite, which is significantly affected by the contact angle between molten LBE and graphite at vacuum. Molten LBE cannot wet graphite well, which requires sufficient infiltration pressure to overcome the capillary force at the interface between molten LBE and graphite for making molten LBE infiltrate into graphite. Moreover, the infiltration behaviors of molten LBE and mercury into graphite are comparable due to their poor wettability of graphite.

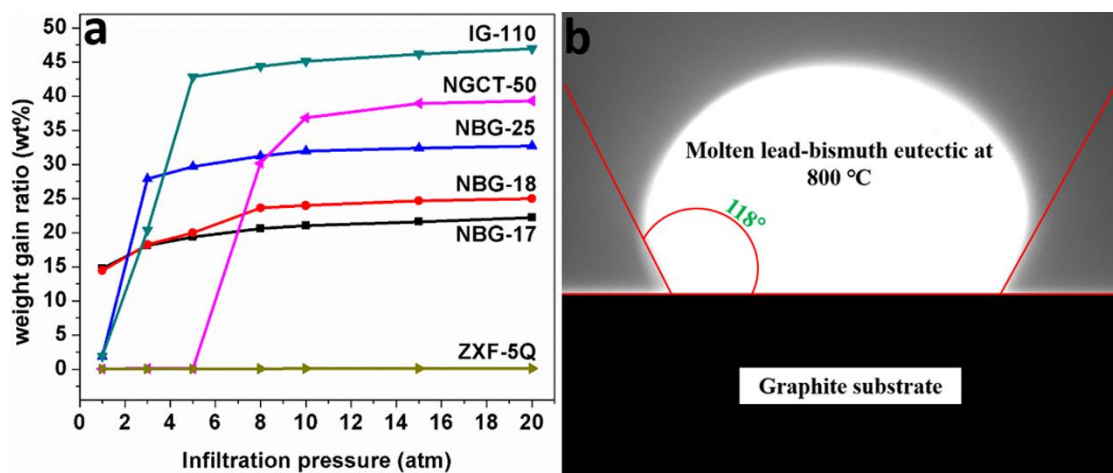


Fig. 2 – a) Molten LBE weight gain ratio of graphite at different infiltration pressures and 800°C; b) image of molten LBE droplet at 800°C on a polished IG-110 graphite substrate.



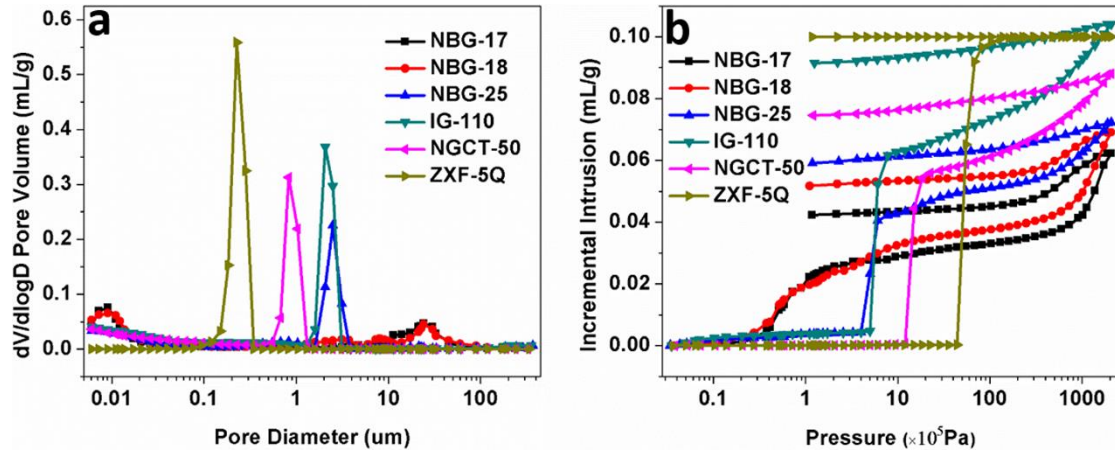


Fig. 3 – Mercury porosimetry results: a) pore size distribution and b) mercury infiltration curves.

Fig. 3a shows the pore size distributions measured in these six grades of graphite, obtained by mercury porosimetry. NBG-17 and NBG-18 have a wide range of pore size distribution, in contrast to the other graphites that have more narrow ranges. NBG-17 and NBG-18 have two pore size distribution peaks at around 20-30  $\mu m$  and below 0.01  $\mu m$ , respectively. The pore size distributions of NBG-25 and IG-110 are concentrated with median pore diameters of 2.49 and 2.06  $\mu m$ , respectively. The ultrafine grained graphites, NGCT-50 and ZXF-5Q have pore size distribution peaks that are below 1  $\mu m$ , and their median pore diameters are 0.83 and 0.23  $\mu m$ , respectively. The results of molten LBE infiltration experiments are consistent with the pore size distributions and the non-wetting of graphite by molten LBE, in that the smaller the graphite pore size is, the more difficult it is for molten LBE infiltrating into the graphite.

The mercury infiltration process generally consists of three stages, and the threshold pressure is a key parameter to distinguish the mercury infiltration process. Fig. 3b shows the mercury infiltration curves obtained for these six grades of graphite. During the first stage, the infiltration pressure is lower than the threshold pressure and very little mercury can infiltrate into the sample. When the infiltration pressure reaches the threshold pressure and increases gradually, a large amount of mercury can infiltrate into the sample, which is the second stage. This is followed by a third stage, in which some

mercury can continue to infiltrate into newly formed pores in the sample, which are usually formed by the collapse of the sample structure under high infiltration pressure. Due to the wide pore size distribution of NBG-17 and NBG-18 (from several microns to tens of microns), their threshold pressures are very low ( $4.12 \times 10^4$  and  $2.76 \times 10^4$  Pa, respectively) and their second stages of mercury infiltration are relatively slow. The pore diameter distributions of the other four grades of graphite are relatively concentrated, so their second stages show a sharp increase in mercury infiltration with pressure. The threshold pressures of NBG-25, IG-110, NGCT-50 and ZXF-5Q are  $3.99 \times 10^5$ ,  $5.01 \times 10^5$ ,  $1.19 \times 10^6$  and  $4.42 \times 10^6$  Pa, respectively. These threshold pressures are higher than those of NBG-17 and NBG-18 as the median pore diameters are much smaller. The total mercury infiltration amounts of NBG-25, IG-110, NGCT-50 and ZXF-5Q are 0.0722, 0.1041, 0.0880 and 0.1001 ml/g, respectively. And the total mercury infiltration amounts of NBG-17 and NBG-18 are only 0.0622 and 0.0691 ml/g, respectively. The ranking of total mercury infiltration amount (NBG-17, NBG-18, NBG-25, NGCT-50, ZXF-5Q and IG-110) corresponds to a ranking of open porosity from low to high and is consistent with the reported graphite densities (Table 1).

In view of the poor wettability of graphite by mercury, the infiltration behavior of mercury into graphite can provide insight into the infiltration behavior of LBE into graphite. The threshold pressures in molten LBE may be deduced using the Washburn equation [28] for the capillary force ( $\Delta P$ ):

$$\Delta P = -\frac{4\gamma\cos\theta}{\delta} \quad (3)$$

where  $\Delta P$ ,  $\gamma$ ,  $\theta$  and  $\delta$  refer to the capillary force, surface tension, contact angle and pore size, respectively.

A scaling factor ( $X$ ), for the threshold pressure in molten LBE, for the same graphite can be defined using equation (4) as

$$X = \frac{\Delta P_{Hg}}{\Delta P_{LBE}} = \frac{\gamma_{Hg} \cos(\theta_{Hg})}{\gamma_{LBE} \cos(\theta_{LBE})} \quad (4)$$

where for graphite and mercury,  $\gamma_{Hg}$  and  $\theta_{Hg}$  are 0.485 N/m and 130° [29], respectively. For molten LBE,  $\gamma_{LBE}$  can be obtained by equation (5):

$$\gamma_{LBE} = (448.5 - 0.0799T) \times 10^{-3} \quad (5) \quad [30]$$

where T is Kelvin temperature.

For the graphite and molten LBE system at 800 °C, the calculated  $\gamma_{LBE}$  and measured  $\theta_{LBE}$  are 0.363 N/m and 118°, respectively, hence the scaling factor  $X$  is 1.83. The obtained threshold pressures in LBE are summarized in Table 2 with the measured threshold pressures in mercury. The calculated threshold pressures of molten LBE are calculated from the measured threshold pressures in mercury by using the scaling factor  $X$  (1.83) and highly consistent with the approximate thresholds indicated by the molten LBE infiltration tests (Fig. 2a).

Table 2 – Threshold pressures for mercury (measured) and LBE (calculated), compared with observed pressures for measurable LBE infiltration (Fig 3a).

Threshold pressure	NBG-17	NBG-18	NBG-25	IG-110	NGCT-50	ZXF-5Q
Mercury (Pa) (measured)	4.12×10 <sup>4</sup>	2.76×10 <sup>4</sup>	3.99×10 <sup>5</sup>	5.01×10 <sup>5</sup>	1.19×10 <sup>6</sup>	4.42×10 <sup>6</sup>
Molten LBE (Pa) (calculated)	2.25×10 <sup>4</sup>	1.51×10 <sup>4</sup>	2.18×10 <sup>5</sup>	2.74×10 <sup>5</sup>	6.50×10 <sup>5</sup>	2.42×10 <sup>6</sup>
Molten LBE (atm) (observed)	<1	<1	<3	<3	>5 and <8	>20
Molten LBE (Pa) (observed)	<1.01×10 <sup>5</sup>	<1.01×10 <sup>5</sup>	<3.03×10 <sup>5</sup>	<3.03×10 <sup>5</sup>	>5.05×10 <sup>5</sup> <8.08×10 <sup>5</sup>	>2.02×10 <sup>6</sup>

Note: Observed threshold pressure for molten LBE in atm is converted to Pa for easy comparison.

Fig. 4 shows fracture surface images of infiltrated graphite samples. LBE appears bright in contrast to graphite, and it is clearly seen that LBE is distributed in and has close contact with the graphite matrix in all grades except ZXF-5Q, even at 20 atm pressure. For NBG-17 and NBG-18, large amounts

of molten LBE can infiltrate even at 1 atm because of their large pore size. For NBG-25 and IG-110, a relatively high infiltration pressure (3 atm) is necessary for molten LBE infiltrating because of their relatively small pore size. The pore diameters of NGCT-50 and ZXF-5Q are less than 1  $\mu\text{m}$  and molten LBE cannot infiltrate into them easily. A high infiltration pressure (8 atm) is necessary to infiltrate molten LBE into NGCT-50 significantly, but even at 20 atm, no obvious LBE can be seen in ZXF-5Q (Fig. 4f). The calculated threshold pressure of molten LBE for ZXF-5Q of  $2.42 \times 10^6$  Pa (Table 2) is much higher than the designed operating pressure of our prototype CHTR. Resistance to infiltration by molten LBE is needed to ensure adequate performance, so the excellent molten LBE barrier property of ZXF-5Q makes it a potential coolant channel material for CHTR. Further studies necessary for it to be used in CHTR include a long-time compatibility test with molten LBE under high temperature irradiation.

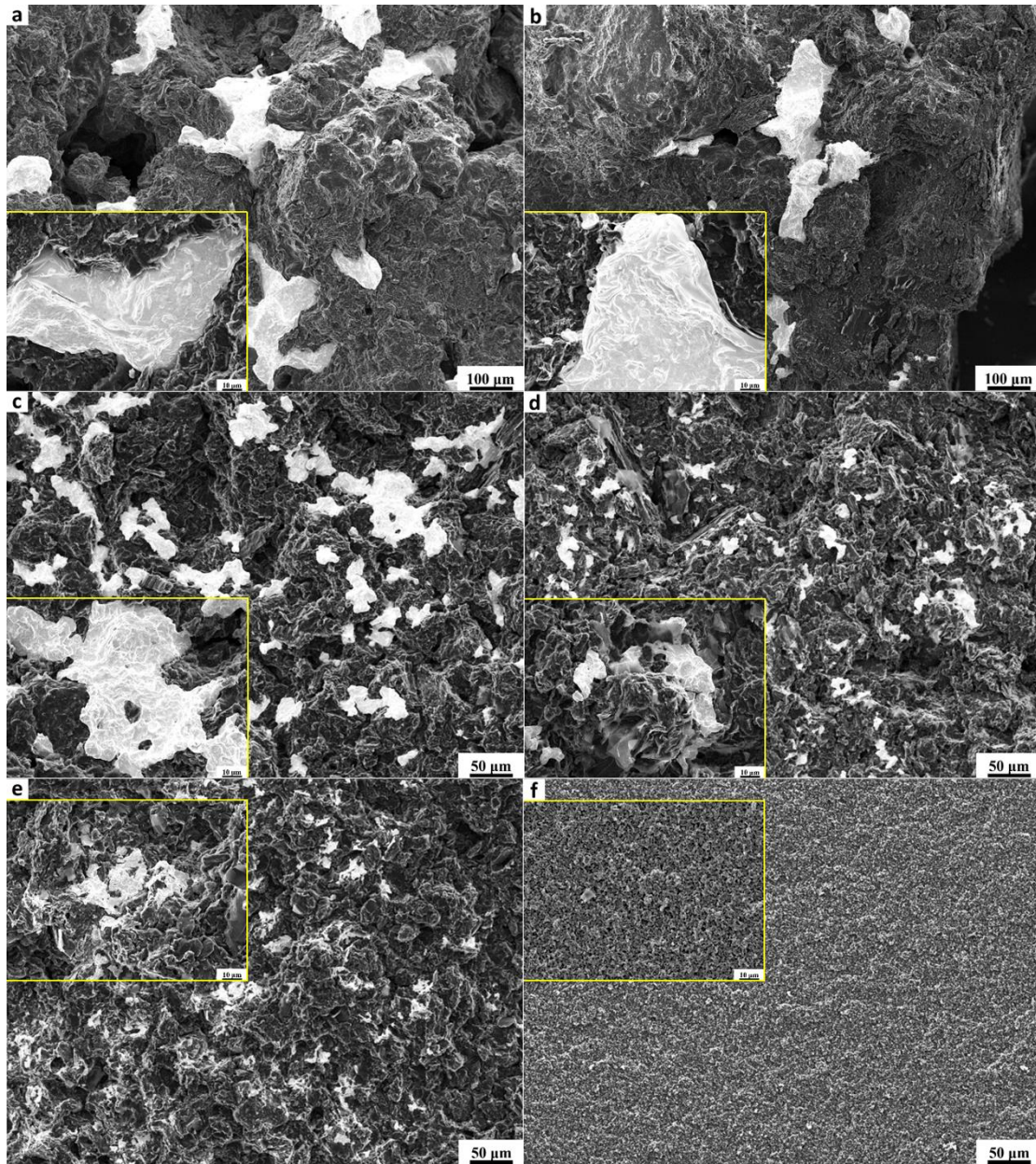


Fig. 4 – Fracture surface images after molten LBE infiltration: a) NBG-17 at 1 atm; b) NBG-18 at 1 atm; c) NBG-25 at 3 atm; d) IG-110 at 3 atm; e) NGCT-50 at 8 atm; and f) ZXF-5Q at 20 atm. (White areas represent the solidified LBE. Insets are higher magnification regions).

### 3.3. *The influence of infiltration process on graphite crystal structures*

To investigate the influence of the LBE infiltration on the crystal structure of graphite, a comparison of the (002) diffraction peaks before and after the molten LBE infiltration at 10 atm are shown in Fig. 5. For the sake of comparison, the cumulative intensities of all spectra have been

normalized to unity. The strong diffraction peak is the (002) diffraction peak of graphite, and the weak diffraction peak is from the solidified LBE. The intensity ratio of these peaks indicates differences in the molten LBE infiltration, and is consistent with the weight gain (Fig. 2a) at 10 atm. There is no LBE diffraction peak detected in the infiltrated ZXF-5Q (Fig. 5f). The (002) diffraction peak of each case is asymmetric. After the molten LBE infiltration, except ZXF-5Q, the (002) peaks significantly shift to a larger  $2\theta$  angle (i.e. decrease spacing of the graphite basal planes) and the FWHMs of the (002) diffraction peak are reduced in comparison to the corresponding raw graphite samples. Interestingly, repeat measurements after 90 days in these five grades of infiltrated graphite showed a further shift to larger  $2\theta$  and a further decrease of the FWHM. The solidified LBE peak shows a shift of similar magnitude after 90 days. It is notable that the position and FWHM of the (002) diffraction peak of ZXF-5Q is nearly unchanged before and after LBE infiltration and shows no obvious change after 90 days. This is consistent with the negligible molten LBE infiltration at 10 atm and demonstrates the repeatability of the diffraction measurements.



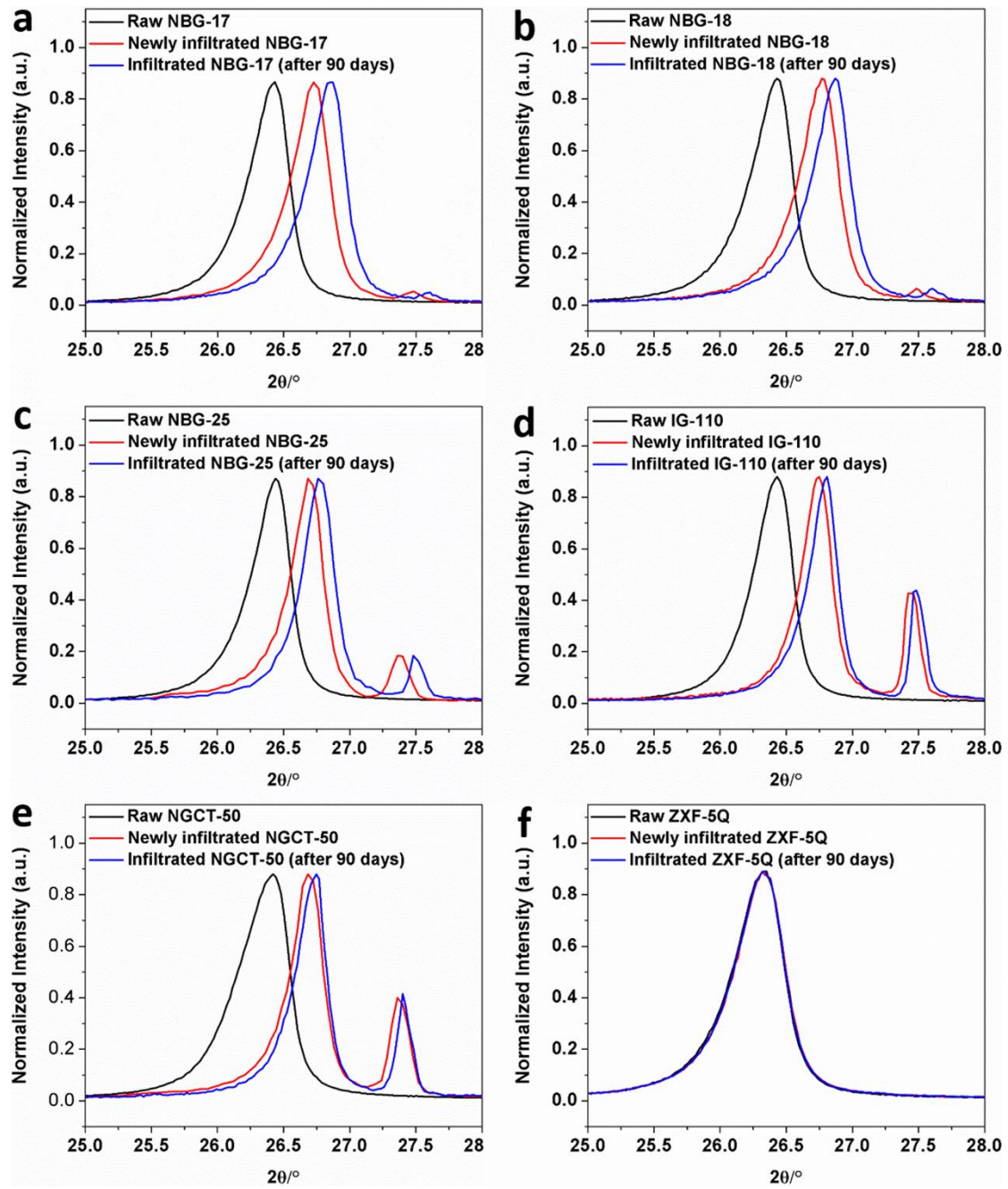


Fig. 5 – Diffraction measurements before and after the molten LBE infiltration at 10 atm. The strong peak is derived from the graphite (002) plane, and the weak peak at higher  $2\theta$  is derived from the LBE: a) NBG-17; b) NBG-18; c) IG-NBG-25; d) IG-110; e) NGCT-50; and f) ZXF-5Q.

The data for the peak positions and FWHMs are summarized in Table 3. From these, the lattice spacing ( $d_{002}$ ) and the mean dimension of crystallite perpendicular to the (002) diffracting plane ( $L_c$ ) are also reported, calculated according to the Bragg diffraction equation (Eq. (6)) and Scherrer equation

(Eq. (7)), respectively:

$$d_{002} = \frac{\lambda}{2\sin\theta} \quad (6)$$

$$\text{and } L_c = \frac{0.9\lambda}{\beta_{002}\cos\theta_{002}} \quad (7).$$

Where  $\lambda$ ,  $\beta$  and  $\theta$  are the X-ray wavelength, diffraction peak width and Bragg angle, respectively.

The  $L_c$  of newly infiltrated graphite is larger than that of raw graphite, and increase further after 90 days in all graphites, except for ZXF-5Q that showed very little change before and after the molten LBE infiltration, which is consistent with the negligible LBE infiltration amount at 10 atm. The  $d_{002}$  of newly infiltrated NBG-25 decreased to 0.33581 nm, which is much smaller than 0.33684 nm of raw NBG-25 and quite close to the 0.33535 nm of natural Ceylon graphite at ambient temperature [31]. The other four grades of graphite into which LBE infiltration occurred developed values of  $d_{002}$  that were smaller than the 0.33354 nm of an ideal graphite crystallite [32]. In addition, the  $L_c$  of all grades of graphite except ZXF-5Q, increased significantly after molten LBE infiltration and increased further after 90 days.



Table 3: Data for  $2\theta$  and FWHM of the (002) diffraction peak (infiltrated with molten LBE at 800 °C and 10 atm) and the calculated  $d_{002}$  and  $L_c$ .

Grade	$2\theta$ of (002) (degree)			$d_{002}$ (nm)			FWHM of (002) diffraction peak (degree)			$L_c$ (nm)		
	RG	NIG	IG90	RG	NIG	IG90	RG	NIG	IG90	RG	NIG	IG90
NBG-17	26.431	26.725	26.851	0.33694	0.33330	0.33177	0.363	0.357	0.352	22.48	22.87	23.20
NBG-18	26.431	26.769	26.871	0.33694	0.33277	0.33153	0.371	0.358	0.348	22.00	22.81	23.47
NBG-25	26.439	26.522	26.765	0.33684	0.33581	0.33281	0.352	0.313	0.303	23.18	26.08	26.95
IG-110	26.432	26.748	26.808	0.33693	0.33302	0.33229	0.348	0.288	0.282	23.45	28.35	28.96
NGCT-50	26.421	26.685	26.746	0.33707	0.33379	0.33305	0.421	0.310	0.292	19.38	26.34	27.96
ZXF-5Q	26.319	26.329	26.339	0.33835	0.33823	0.33810	0.437	0.432	0.431	18.67	18.89	18.93

Note: RG=Raw graphite; NIG= Newly infiltrated graphite; IG90= Infiltrated graphite stored for 90 days.

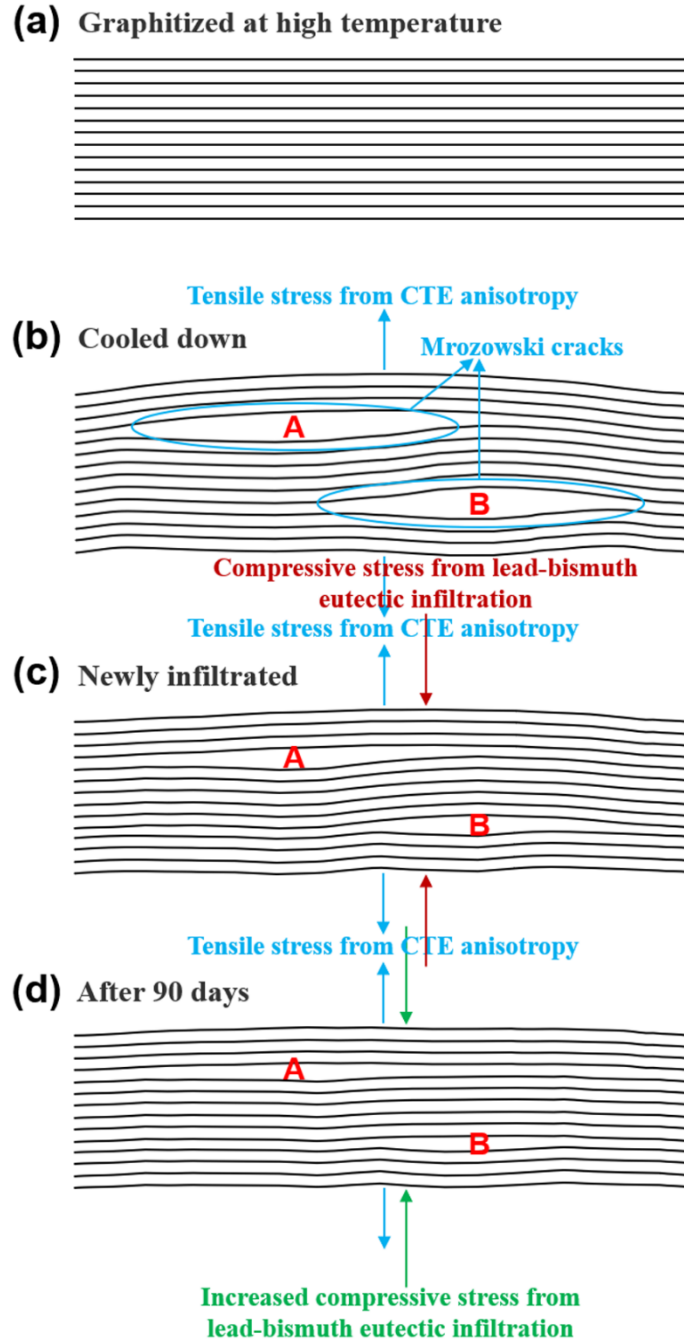


Fig. 6 – The generation of Mrozowski cracks and the fluctuation of  $d_{002}$  during the cooling process after graphitization and the influence of molten LBE infiltration on the Mrozowski cracks and  $d_{002}$ . (a) graphite crystallite with high graphitization degree; (b) the Mrozowski cracks caused by the tensile stress perpendicular to the (002) diffracting plane at ambient temperature; (c) the closure of Mrozowski cracks and the decrease of  $d_{002}$  fluctuation, which are caused by the compressive stress derived from molten LBE infiltration; (d) the further closure of Mrozowski cracks and the further decrease of  $d_{002}$

fluctuation, which are caused by the increased compressive stress derived from subsequent solid-state phase transformation expansion of LBE during the 90 days preservation process.

A proposed explanation for the observed changes in the diffraction data is illustrated in Fig. 6. The proposed explanation herein is inspired by the relevant mechanism proposed by previous work [15]. Fig. 6 is drawn based on previous work [15] and has been appropriately modified according to the experiment content of this work. Initially (Fig.6a), a well graphitized structure develops in the graphitization process at high temperature. During the subsequent cooling, the significant crystal anisotropy of thermal expansion results to a tensile strain perpendicular to the (002) diffracting plane, which is responsible for the generation of Mrozowski cracks [15, 33-35] and a tensile residual stress that affects  $d_{002}$  (Fig. 6b). The CTE of the solid LBE is on the order of  $10^{-5}/K$  [30], which is much higher than  $10^{-6}/K$  of nuclear graphite. On cooling after LBE infiltration, the mismatch of CTE between the solidified LBE and the graphite makes the graphite matrix subjected to compressive stress perpendicular to the (002) diffracting plane from the LBE particles, which leads to the closure of Mrozowski cracks and the decrease of  $d_{002}$  fluctuation as shown in Fig. 6c. This compression causes the value of  $d_{002}$  to be lower than the ideal plane spacing for graphite. During the 90 days storage, the expansion of LBE particles, which derives from its solid-state phase transformation from  $\beta$ -phase to  $\gamma$ -phase [36], introduces a compressive stress that results in a further decrease of  $d_{002}$  fluctuation (Fig. 6d) and would also tend to further closure of Mrozowski cracks. The closure of Mrozowski cracks is conducive to increase the  $L_c$  of graphite matrix, which is shown by the decrease of FWHM of (002) diffraction peak.

### ***3.4. Chemical compatibility of molten LBE with graphite***

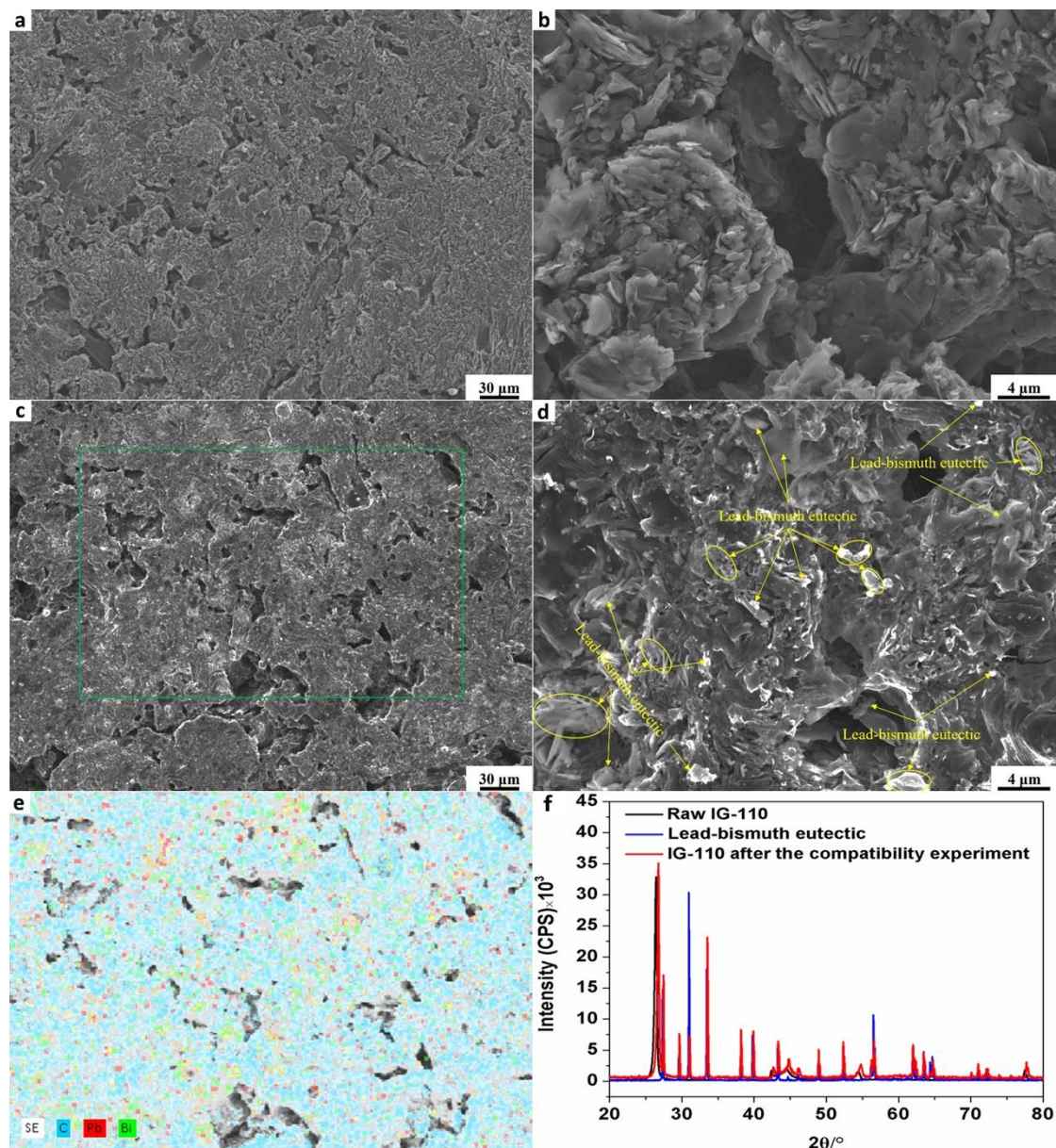


Fig. 7 – Surface images of polished IG-110 graphite before (a, b) and after (c, d) the compatibility experiment; (e) EDS map of the selected area in Fig. 7C; (f) XRD spectra of raw IG-110 graphite, LBE and IG-110 graphite after the compatibility experiment.

Surface images of the mechanically polished IG-110 graphite, before and after the compatibility experiment, are shown in Fig. 7. Some large pores over 10  $\mu\text{m}$  in size (Fig. 7a and b) are observed. These were not indicated by the mercury injection test, but such pores were observed on the fracture surface (before infiltration, Fig. 1d). Mercury porosimetry measures only the size of the channels

connecting large pores [37], and such channels determine the threshold pressures and influence the infiltration process. Some molten LBE penetrated the large surface pores (Fig. 7c and d), as shown by the EDS map (Fig. 7e), but otherwise the surface of graphite shows no obvious corrosion and the weight gain was negligible (0.64 wt%). The XRD spectra (Fig. 7f) show no new phase formed, but the graphite diffraction peaks shifted slightly to larger  $2\theta$  angle, which indicates there was some infiltration of molten LBE into the surface. The experimental results discussed above indicate that graphite is resistant to the corrosion from molten LBE even at 800 °C for 1000 hours, which has preliminarily verified the superiority and feasibility of nuclear graphite as coolant channel material for CHTR. Of course, it is still necessary to investigate the chemical and structural stability of graphite under the condition of longer time and higher temperature molten LBE corrosion coupled with irradiation before the formal application of graphite coolant channels in CHTR.

#### **4. Conclusion**

The infiltration of molten LBE into six grades of commercial nuclear graphite has been investigated at 800°C under a range of pressures. The ultrafine grained graphite, ZXF-5Q, has the best barrier property to molten LBE among all graphites, which is ascribed to its smallest pore size. A compressive stress, caused by the mismatch of CTE between LBE and graphite, may be responsible for the reduction in the (002) plane spacing and the increase of mean crystallite dimension perpendicular to the (002) diffracting plane that are observed after LBE infiltration. A further increase in compressive stress, which derives from subsequent solid-state phase transformation expansion of LBE, causes the further decrease in the (002) plane spacing and the increase of mean crystallite dimension. Chemical stability of graphite is demonstrated in molten LBE at 800 °C for 1000 hours. The findings of this work shed light on selecting qualified nuclear graphite to act as coolant channel

material for CHTR, and thus, may promote the development of CHTR.

### **Declaration of competing interest**

The authors declare that they have no known competing financial interests or personal relationships that could have appeared to influence the work reported in this paper.

### **Credit author statement**

**Zhao He:** Conceptualization, Investigation, Formal analysis, Data curation, Writing - original draft, Writing review & editing, Validation, Methodology. **Zhanjun Liu:** Funding acquisition, Supervision, Validation, Visualization, Writing - review & editing. **T. James Marrow:** Writing - review & editing. **Jinliang Song:** Funding acquisition, Resources.

### **Acknowledgments**

Great thanks to the National Natural Science Foundation of China (No. 91860116 and 52072397) for its financial support for this work. This manuscript is written whilst Zhao He was an Academic Visitor at University of Oxford with the financial support of China Scholarship Council (File No. 201904910864).

### **References**

- [1] I.V. Dulara, R.K. Sinha, High temperature reactors, J. Nucl. Mater. 383(1-2) (2008) 183-188.
- [2] X. Huang, X. Gong, M. Song, J. Chen, F. Hu, Y. Yin, et al., Liquid metal embrittlement susceptibility of a high-entropy alloy exposed to oxygen-depleted liquid lead-bismuth eutectic at 250 and 350 °C, J. Nucl. Mater. 528 (2020).
- [3] X. Gong, F. Hu, J. Chen, H. Wang, H. Gong, J. Xiao, et al., Effect of temperature on liquid metal embrittlement susceptibility of an Fe10Cr4Al ferritic alloy in contact with stagnant lead-bismuth eutectic, J. Nucl. Mater. 537 (2020).
- [4] Z. He, L. Gao, W. Qi, B. Zhang, X. Wang, J. Song, et al., Molten FLiNaK salt infiltration into degassed nuclear graphite under inert gas pressure, Carbon 84 (2015) 511-518.
- [5] Z. He, P. Lian, J. Song, D. Zhang, Z. Liu, Q. Guo, Microstructure and properties of fine-grained isotropic graphite based on mixed fillers for application in molten salt breeder reactor, J. Nucl. Mater. 511 (2018) 318-327.
- [6] Z. He, P. Lian, Y. Song, Z. Liu, J. Song, J. Zhang, et al., Improving molten fluoride salt and Xe<sup>135</sup> barrier property of nuclear graphite by phenolic resin impregnation process, J. Nucl. Mater. 499 (2018) 79-87.
- [7] Z. He, P. Lian, Y. Song, Z. Liu, J. Song, J. Zhang, et al., Protecting nuclear graphite from liquid fluoride salt and oxidation by SiC coating derived from polycarbosilane, J. Eur. Ceram. Soc. 38(2) (2018) 453-462.
- [8] Z. He, Z. Liu, J. Song, P. Lian, Q. Guo, Fine-grained graphite with super molten salt barrier property produced from filler

of natural graphite flake by a liquid-phase mixing process, *Carbon* 145 (2019) 367-377.

- [9] Z. He, J. Song, P. Lian, D. Zhang, Z. Liu, Excluding molten fluoride salt from nuclear graphite by SiC/glassy carbon composite coating, *Nucl. Eng. Technol.* 51(5) (2019) 1390-1397.
- [10] H. Zhao, Z. He, Z. Liu, J. Song, D.K.L. Tsang, H. Zhang, Self-sintered nanopore-isotropic graphite derived from green pitch coke for application in molten salt nuclear reactor, *Ann. Nucl. Energy* 131 (2019) 412-416.
- [11] Z. He, J. Song, Z. Wang, X. Guo, Z. Liu, T.J. Marrow, Comparison of ultrafine-grain isotropic graphite prepared from microcrystalline graphite and pitch coke, *Fuel* 290 (2021).
- [12] Z. He, P. Lian, X. Guo, J. Song, X. Yan, Z. Liu, et al., Ultrafine-grained graphite prepared from filler of onion-like carbon spheres via a liquid mixing process for using in molten salt reactor, *J. Nucl. Mater.* 547 (2021).
- [13] X. Yang, S. Feng, X. Zhou, H. Xu, T.K. Sham, Interaction between nuclear graphite and molten fluoride salts: a synchrotron radiation study of the substitution of graphitic hydrogen by fluoride ion, *J. Phys. Chem. A* 116(3) (2012) 985-989.
- [14] H. Wu, F. Carotti, R. Gakhar, N. Patel, R.O. Scarlat, Fluorination of nuclear graphite IG-110 in molten 2LiF-BeF<sub>2</sub> (FLiBe) salt at 700 °C, *J. Fluorine Chem.* 211 (2018) 159-170.
- [15] Z.T. He, L.N. Gao, X. Wang, B.L. Zhang, W. Qi, J.L. Song, et al., Improvement of stacking order in graphite by molten fluoride salt infiltration, *Carbon* 72 (2014) 304-311.
- [16] W. Qi, Z. He, H. Tang, B. Zhang, C. Zhang, L. Gao, et al., Effects of FLiNaK infiltration on thermal expansion behavior of graphite, *J. Mater. Sci.* 52(8) (2016) 4621-4634.
- [17] C. Zhang, Z. He, Y. Gao, H. Tang, W. Qi, J. Song, et al., The effect of molten FLiNaK salt infiltration on the strength of graphite, *J. Nucl. Mater.* 512 (2018) 37-45.
- [18] W. G. Stroud, The Penetration of Graphites of Different Purities by Lead-Bismuth Eutectic, USAEC Report CP-2242, University of Chicago, Sept. 25, 1944.
- [19] R.E. Nightingale (Ed.), Nuclear Graphite, Chapter 15—Graphite-Metal and Graphite-Molten Salt Systems, Academic Press Inc, New York (1962), pp. 445-463.
- [20] R. Keen and R. Cygan, High-temperature Materials Studies Semi-Annual Progress Report, July-December 1952, USAEC Report NAA-SR-231, North American Aviation, Inc., May 1953.
- [21] A.K. Sengupta, R.K. Bhagat, A. Laik, G.B. Kale, T. Jarvis, S. Majumdar, et al., Out-of-pile chemical compatibility of Pb-Bi eutectic alloy with Graphite, *Int. J. Mater. Res.* 97(6) (2006) 834-837.
- [22] P. Chakraborty, A. Ghosh, G.K. Dey, Compatibility of Lead-Bismuth Eutectic with SiC-Coated Graphite at Elevated Temperature, *Metall. Mater. Trans. B* 48(1) (2016) 1-5.
- [23] TANG Hui, HE Zhoutong, ZHANG Can, WANG Xue, XIA Huihao, Equipment design and experiment of compatibility test of nuclear graphite and molten salt, *Nucl. Tech.* 41(7) (2018) 070605.
- [24] G. Chen, N. Ju, Y. Lei, D. Wang, Q. Zhu, T. Li, Corrosion behavior of 410 stainless steel in flowing lead-bismuth eutectic alloy at 550 °C, *J. Nucl. Mater.* 522 (2019) 168-183.
- [25] J. Fang, L. Sun, Q. Qi, J. Zhang, C. Liu, Microstructure evolution and mechanical properties of porous Si<sub>3</sub>N<sub>4</sub> and dense Si<sub>3</sub>N<sub>4</sub> joints bonded using CaO–Li<sub>2</sub>O–Al<sub>2</sub>O<sub>3</sub>–SiO<sub>2</sub> glass-ceramic, *J. Eur. Ceram. Soc.* 39(15) (2019) 4545-4553.
- [26] L. Sun, C. Liu, S. Guo, J. Fang, D. Wang, J. Zhang, Wetting and joining of porous Si<sub>3</sub>N<sub>4</sub> and dense Si<sub>3</sub>N<sub>4</sub> ceramics with in-situ formed β-spodumene/spinel glass-ceramic interlayer, *Appl. Surf. Sci.* 517 (2020).
- [27] F.W. Jones, The Measurement of Particle Size by the X-Ray Method, *Proc. Roy. Soc. A* 166(924) (1938) 16-43.
- [28] E.W. Washburn, The Dynamics of Capillary Flow, *Phys. Rev.* 17(3) (1921) 273-283.
- [29] H. Giesche, Mercury Porosimetry: A General (Practical) Overview, *Part. Part. Syst. Char.* 23(1) (2006) 9-19.
- [30] OECD/NEA (2015), Handbook on Lead-bismuth Eutectic Alloy and Lead Properties, Materials Compatibility, Thermal-hydraulics and Technologies-Edition 2015, Nuclear Science, OECD Publishing, Paris.
- [31] W.L. Bragg, The conversion factor for kX units to ångström units, *J. Sci. Instrum.* 24 (1947) 27-27.

- [32] N. Simos, P. Hurh, N. Mokhov, M. Snead, M. Topsakal, M. Palmer, et al., Low-temperature proton irradiation damage of isotropic nuclear grade IG-430 graphite, *J. Nucl. Mater.* 542 (2020).
- [33] Kelly BT. *Physics of graphite*. London: Applied Science; 1981. p. 35–48.
- [34] K. Wen, J. Marrow, B. Marsden, Microcracks in nuclear graphite and highly oriented pyrolytic graphite (HOPG), *J. Nucl. Mater.* 381(1-2) (2008) 199-203.
- [35] S. Mrozowski, *Phys. Rev.* 86 (1952) 622.
- [36] H. Glasbrenner, F. Gröschel, H. Grimmer, J. Paturski, M. Rohde, Expansion of solidified lead bismuth eutectic, *J. Nucl. Mater.* 343(1-3) (2005) 341-348.
- [37] Q. Huang, H. Tang, Porosity analysis of superfine-grain graphite IG-110 and ultrafine-grain graphite T220, *Mater. Sci. Technol.* 35(8) (2019) 962-968.